Light and motion in SDSS Stripe 82: the catalogues

D. M. Bramich,[1,2]★ S. Vidrih,[1,3] L. Wyrzykowski,[1] J. A. Munn,[4] H. Lin,[5] N. W. Evans,[1] M. C. Smith,[1] V. Belokurov,[1] G. Gilmore,[1] D. B. Zucker,[1] P. C. Hewett,[1] L. L. Watkins,[1] D. C. Faria,[1] M. Fellhauer,[1] G. Miknaitis,[5] D. Bizyaev,[6] Ž. Ivezić,[7] D. P. Schneider,[8] S. A. Snedden,[6] E. Malanushenko,[6] V. Malanushenko[6] and K. Pan[6]

[1]*Institute of Astronomy, University of Cambridge, Madingley Road, Cambridge CB3 0HA*
[2]*Isaac Newton Group of Telescopes, Apartado de Correos 321, E-38700 Santa Cruz de la Palma, Canary Islands, Spain*
[3]*Astronomisches Rechen-Institut/Zentrum für Astronomie der Universität Heidelberg, Mönchhofstrasse 12-14, 69120 Heidelberg, Germany*
[4]*US Naval Observatory, Flagstaff Station, 10391 W. Naval Observatory Road, Flagstaff, AZ 86001-8521, USA*
[5]*Fermi National Accelerator Laboratory, Box 500, Batavia, IL 60510, USA*
[6]*Apache Point Observatory, 2001 Apache Point Road, Sunspot, NM 88349, USA*
[7]*Department of Astronomy, University of Washington, Seattle, WA 98155, USA*
[8]*Department of Astronomy and Astrophysics, The Pennsylvania State University, University Park, PA 16802, USA*

ABSTRACT

We present a new public archive of light-motion curves in Sloan Digital Sky Survey (SDSS) Stripe 82, covering $99°$ in right ascension from $\alpha = 20^h7$ to 3^h3 and spanning $2°52$ in declination from $\delta = -1°26$ to $1°26$, for a total sky area of $\sim$249 deg^2. Stripe 82 has been repeatedly monitored in the u, g, r, i and z bands over a seven-year baseline. Objects are cross-matched between runs, taking into account the effects of any proper motion. The resulting catalogue contains almost 4 million light-motion curves of stellar objects and galaxies. The photometry are recalibrated to correct for varying photometric zero-points, achieving $\sim$20 and 30 mmag rms accuracy down to 18 mag in the g, r, i and z bands for point sources and extended sources, respectively. The astrometry are recalibrated to correct for inherent systematic errors in the SDSS astrometric solutions, achieving $\sim$32 and 35 mas rms accuracy down to 18 mag for point sources and extended sources, respectively.

For each light-motion curve, 229 photometric and astrometric quantities are derived and stored in a higher level catalogue. On the photometric side, these include mean exponential and point spread function (PSF) magnitudes along with uncertainties, rms scatter, χ^2 per degree of freedom, various magnitude distribution percentiles, object type (stellar or galaxy), and eclipse, Stetson and Vidrih variability indices. On the astrometric side, these quantities include mean positions, proper motions as well as their uncertainties and χ^2 per degree of freedom. The light-motion curve catalogue presented here is complete down to $r \sim 21.5$ and is at present the deepest large-area photometric and astrometric variability catalogue available.

Key words: catalogues – astrometry – stars: variables: others – Galaxy: stellar content – galaxies: photometry.

1 INTRODUCTION

One meaning of the verb 'to vary' is to change in amount or level, especially from one occasion to another. In astronomy, there are many types of temporal variability. Stars may change in brightness, in which case they are termed 'variables', or they may change position on the sky, in which case they have a proper motion. Over a sufficiently long period of time, the shapes of constellations change.

Galaxies exhibit variability across the electromagnetic spectrum since their emission is made up of the radiation from billions of sources, although their most obvious source of variation comes from active galactic nuclei or supernovae. Transient events, such as gamma-ray bursts, or microlensing events, are intrinsically variable. Solar system objects from planets to asteroids drift slowly across the sky, waxing and waning on various time-scales. In fact, at some level, everything in the sky is variable.

The introduction of CCD detectors to astronomy greatly enhanced the ability to conduct variability surveys. The extension of CCD cameras to mosaic and wide-field formats along with the

★E-mail: dmb@ing.iac.es

exponential progression of computing power have allowed the subsequent development of more ambitious surveys reaching to deeper magnitudes, higher cadences and larger sky areas. For more details we direct the reader to Becker et al. (2004) who present a clear summary of modern variability surveys. In this work we concentrate on optical photometric and astrometric variability (hence 'light and motion') over a ∼249 deg² patch of sky.

Large sky surveys such as the Sloan Digital Sky Survey (SDSS; York et al. 2000) have in many ways revolutionized our knowledge of the Universe. SDSS has imaged approximately a quarter of the sky in five photometric wavebands. The exploitation of this impressive data set has resulted in hundreds of publications covering a wide range of astronomical topics, from the structure of the Milky Way to the mapping of a large fraction of the Universe. The bulk of these data, however, contain only single measurements of objects from the north Galactic cap with no information on possible photometric variability or astrometric motion. Substantial efforts have been made by Munn et al. (2004) (see also Gould & Kollmeier 2004) to measure proper motions by matching SDSS data from the north Galactic cap with the USNO-B catalogue (Monet et al. 2003). The resultant proper motion catalogue is 90 per cent complete down to $g = 19.7$ with the magnitude limit being set by the USNO-B catalogue faint magnitude limits.

One of the primary goals of the SDSS is the study of the variable sky (Adelman-McCarthy et al. 2007) of which our knowledge is still very incomplete (Paczyński 2000). To this end, the SDSS has repeatedly imaged a 300-deg² area, the so-called Stripe 82, during the later half of each year since 1998. In 2005, the SDSS-II Supernova Survey (Frieman et al. 2008) started with the aim of detecting Type I supernovae in Stripe 82, greatly improving the cadence of measurements within the stripe. By averaging a subset of the repeated observations of unresolved sources in Stripe 82, Ivezić et al. (2007) built a standard star catalogue containing ∼1 million nonvariable sources with r-band magnitudes in the range 14–22, by far the deepest and most numerous set of photometric standards available. Using these same multi-epoch photometric data, Sesar at al. (2007) analysed the photometric variability for ∼1.4 million unresolved sources in the stripe, drawing interesting conclusions on the spatial distribution of RR Lyrae stars and the variability of quasars.

Here we present a new public archive of light-motion curves in SDSS Stripe 82. The archive has been constructed from the set of high-precision multi-epoch photometric and astrometric measurements made in the stripe since the first SDSS runs in 1998 until the end of 2005. In constructing the catalogue, we only use measurements of objects that are cleanly detected in individual SDSS runs. The catalogue contains almost 4 million objects, galaxies and stars, and is complete down to magnitude 21.5 in u, g, r and i, and to magnitude 20.5 in z. Each object has its proper motion calculated based only on the multi-epoch SDSS J2000 astrometric measurements. The catalogue reaches almost 2 mag deeper than the SDSS/USNO-B catalogue, making it the deepest large-area photometric and astrometric catalogue available.

The catalogue comes in two flavours, the light-motion curve catalogue (LMCC), which contains the set of individual light-motion curves, where measured quantities for each object are listed as a function of waveband and epoch, and the higher level catalogue (HLC), which presents a set of derived quantities for each light-motion curve. For many purposes, it is more convenient to work with the HLC, especially for selecting subsets of interesting objects. The construction, calibration and format of the LMCC are discussed in Section 2, and the HLC is described in Section 3. Between the two subcatalogues, there is all the necessary infor-

mation available to explore the photometric and astrometric variability of ∼249 deg² of equatorial sky. In Section 4, we investigate the quality of the photometric and astrometric properties of our catalogues by comparing them against suitable external catalogues, and we analyse the behaviour of our proper motion uncertainties.

2 THE LIGHT-MOTION CURVE CATALOGUE

2.1 Stripe 82 data

The SDSS photometric camera is mounted on a 2.5 m dedicated telescope at the Apache Point Observatory, New Mexico. It consists of a photometric array of 30 SITe/Tektronix CCDs, each of size 2048×2048 pixels, arranged in the focal plane of the telescope in six columns of five chips each (Gunn et al. 1998, 2006) with a space of approximately one chip width between columns. Each row of six chips is positioned behind a different filter so that SDSS imaging data are produced in five wavebands, namely u, g, r, i and z (Fukugita et al. 1996; Smith at al. 2002). The camera operates in time-delay-and-integrate (TDI) drift-scan mode at the sidereal rate and the chip arrangement is such that two scans cover a filled stripe 2°.54 wide, with ∼1 arcmin overlap between chip columns in the two scans. In addition, the camera contains an array of 24 CCDs with 400×2048 pixels which enable observations of bright astrometric reference stars for subsequent astrometry and focus monitoring.

The images are automatically processed through specialized pipelines (Lupton, Gunn & Szalay 1999; Hogg et al. 2001; Lupton et al. 2001; Stoughton et al. 2002; Ivezić et al. 2004) producing corrected images, object catalogues, astrometric solutions, calibrated fluxes and many other data products. The object catalogues, which include the calibrated photometry and astrometry, are stored in FITS binary table format (Wells, Greisen & Harten 1981; Cotton, Tody & Pence 1995; Hanisch et al. 2001) and referred to as 'tsObj' files. It is these object catalogues that we have used to construct the LMCC.

The SDSS Stripe 82 is defined as the region spanning 8 h in right ascension (RA) from $\alpha = 20^h$ to 4^h and 2°.5 in declination (Dec.) from $\delta = -1°.25$ to $1°.25$. The stripe consists of two scan regions referred to as the north and south strips. Both the north and south strips have been repeatedly imaged from 1998 to 2005, between June and December of each year, with 62 of the 134 imaging runs obtained in 2005 alone (this large sampling rate was produced by the start of the SDSS-II Supernova Survey). A specific imaging run may cover all of one strip or some fraction of the area, and images of the same patch of sky are never taken more than once per night. Hence the exact temporal coverage and cadence of the light-motion curves in the catalogue are strong functions of celestial position. In Table 1, we list the SDSS imaging runs included in the LMCC organized by the month and year of observation. Not all scans of Stripe 82 were included in our analysis due to failures in the SDSS FRAMES pipeline (Lupton et al. 2001) when processing a run or failure of our calibration routines to produce photometric zero-points (see Section 2.2).

2.2 Further photometric calibrations

The Stripe 82 data set includes 62 'standard' SDSS imaging runs which were observed under photometric conditions and which were photometrically calibrated using the standard SDSS pipelines

Table 1. The list of SDSS imaging runs included in the LMCC. All runs were processed with version 40 of the SDSS FRAMES pipeline except those runs marked with an asterisk, which were processed with version 41. Runs 4203 and 5823 (underlined) are the reference runs used for the astrometric calibrations (see Section 2.4).

Year	Month	North strip runs	South strip runs
1998	September	94	125
1999	October	1033	1056
2000	September	1752	–
2000	October	–	1755
2000	November	–	1894
2001	June	2385	–
2001	September	2570, 2578, 2589	2579, 2583, 2585
2001	October	2649, 2650, 2659, 2662, 2677	–
2001	November	2700, 2708, 2728, 2738	2709
2001	December	2768, 2820	–
2002	January	2855, 2861, 2873	2886
2002	September	–	3325*
2002	October	3362, 3384, 3437	3355, 3360*, 3388, 3427, 3430, 3434, 3438
2002	November	3461	3460, 3465
2003	September	4128, 4153, 4157	4136, 4145
2003	October	4184, 4188, 4198, 4207	4187, 4192, <u>4203</u>
2003	November	4253	4247, 4263, 4288
2004	August	4797	–
2004	September	4858	–
2004	October	4868, 4874, 4895, 4905, 4917	–
2004	November	4933, 4948	4930
2004	December	–	5042, 5052
2005	September	5566, 5603, 5610, 5622, 5633, 5642, 5658	5582, 5597, 5607, 5619, 5628, 5637, 5646, 5666
2005	October	5709, 5719, 5731, 5744, 5759, 5765, 5770, 5777, 5781, 5792, 5800	5675, 5681, 5713, 5729, 5730, 5732, 5745, 5760, 5763, 5771, 5776, 5782, 5786, 5797
2005	November	5813, <u>5823</u>, 5842, 5865, 5866, 5872, 5878, 5898, 5902, 5918	5807, 5820, 5836, 5847, 5853, 5870, 5871, 5882, 5889, 5895, 5905, 5924

(Tucker et al. 2006). We use these standard runs to construct a reference catalogue of bright star fluxes, from which we can both improve the photometric calibrations of the standard runs, as well as derive photometric calibrations for the Stripe 82 supernova imaging runs from 2005, which were generally observed under non-photometric conditions.

To construct the reference catalogue, we start with a set of bright, unsaturated stars, with $14 < r < 18$, taken from a set of high-quality runs acquired over an interval of less than twelve months (2659, 2662, 2738, 2583, 3325, 3388). We then match the individual detections of these stars in each of the 62 standard runs, using a matching radius of 1 arcsec. On average, there are 10 independent measurements of each star among the standard runs, and we only include in the reference catalogue stars with five or more measurements. We then compute the unweighted mean of the independent flux measurements of each star and adopt that mean flux in our reference catalogue. Note that we specifically use the fluxes measured in the so-called SDSS 'aperture 7', which has a radius of 7.43 arcsec; this aperture is typically adopted in the SDSS as a reference aperture appropriate for isolated bright star photometry.

These reference catalogue stars are used to recalibrate the standard runs, as well as to calibrate the 2005 supernova data. For the supernova runs, we first adopt a sensible but arbitrary zero-point for the purposes of generating the initial tsObj files using standard SDSS pipeline tools. We then match the object detections in each run to the reference catalogue, and compute the median fractional flux offset of the reference stars in the individual run relative to the reference catalogue.[1] These median offsets are computed in two iterations. We first calculate the median fractional offset for each run in bins of 0°.0208 in Dec., i.e. 120 bins over the width of Stripe 82, or about 10 bins per CCD width. This exercise is designed to correct flat-fielding errors for a given run. Note that these errors would only depend on Dec. because the SDSS employs a drift-scan camera, and the scan direction for Stripe 82 is in the RA direction. After correcting for the Dec.-dependent offsets, we then recompute the median fractional flux offsets for each field along a given run (each SDSS field is 0°.15 long in RA). This additional field-by-field offset corrects for any temporal variations in the photometric zero-point of a given run, which are due to transparency/extinction changes over the course of a nominally photometric night.

Flux offsets for a certain waveband were only applied to objects assigned to a bin with at least nine reference catalogue stars in order to guarantee the accuracy of the derived flux offset. In practice, this extra restriction only affects the photometry of objects in the *u* band, and in other wavebands when the atmospheric transparency is

---

[1] The *u*-band images possess a significantly poorer signal-to-noise ratio than the other bands and the use of reference catalogue stars that have a magnitude fainter than 18 *before* calibration (due to higher than usual extinction) degrades the determination of the derived flux offsets. The flux offsets for the *u* band have therefore been determined using only the reference catalogue stars with an uncalibrated magnitude brighter than 18 in each run.
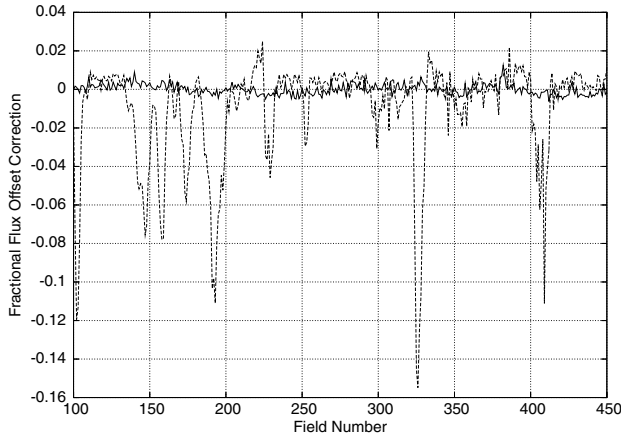
Figure 1. Plot of the median fractional flux offset of the reference stars relative to the reference catalogue as a function of field number for runs 94 (solid line) and 5853 (dashed line). For both runs we show the offsets for camera column 1 and the *r* band. Run 94 is a typical pre-2005 run observed under photometric conditions and run 5853 is a typical 2005 supernova run observed under non-photometric conditions.

low. We use a photometric calibration tag (see Table 3) to monitor whether or not a flux offset has been applied to the photometry of a particular object at a certain epoch in a specific waveband. The final tsObj files used for subsequent analyses therefore have both these Dec.-dependent and field-dependent flux offsets removed for most object records. We find that for the standard SDSS runs, the fractional flux offset corrections, which we refer to as photometric zero-points, are about 1–2 per cent, which sets the typical scale of these residual errors in the standard SDSS calibration procedures. Fig. 1 shows the fractional flux offset corrections as a function of SDSS field number (an arbitrary coordinate along RA assigned to image sections from the same run) for a typical photometric run (94) and a typical non-photometric run (5853).

2.3 Catalogue construction

The object catalogues (tsObj files) contain quality and type flags for each object record to aid in the selection of 'good' measurements and specific data samples. In the LMCC, we only accept object records classified as galaxies/non-PSF-like objects (tsObj file tag OBJC_TYPE = 3) or stars/PSF-like objects (tsObj file tag OBJC_TYPE = 6), and the object must have no child objects (tsObj file tag NCHILD = 0; Stoughton et al. 2002). We then require that an object record satisfies all of a set of constraints in at least one waveband. The first of these constraints is that a photometric zero-point, calculated using the method described in Section 2.2, has been applied to the object record, and that the object record has an *uncalibrated* point spread function (PSF) magnitude (tsObj file tag PSFCOUNTS) brighter than 21.5 for the bands *u, g, r* and *i*, or brighter than 20.5 for the *z* band. These limits were chosen to ensure that any photometric measurement in the LMCC has a signal-to-noise ratio of at least 5 in at least one waveband. In Table 2, we list the remaining set of constraints to be satisfied in at least one waveband in order for an object record to be included in the LMCC.

We apply one final constraint on the quality of an object record in order to avoid the inclusion of cosmic ray events in our catalogue. If an object record satisfies all of the above constraints in one waveband only, then it is accepted only if the tsObj file tag FLAGS2 for that waveband does not contain the hexadecimal bit 0x1000000 (flag name MAYBE_CR), the presence of which indicates that the object is possibly a cosmic ray.

In order to construct the light-motion curves, we processed each run in turn, starting with the 2005 runs which were closely spaced in time. For each object record in the current run satisfying our quality and type constraints, we used the following algorithm to process the record.

(i) We define a subset of objects with light-motion curves from the current catalogue that have mean positions inside a 1-arcmin box centred on the position of the current object record.

(ii) We calculate an expected position at the epoch of the current object record for each object in the subset using one of two

Table 2. The list of extra constraints that all need to be satisfied in at least one waveband in order for an object record to be included in the LMCC.

| Tag name in tsObj file	Relation	Flag (hexadecimal bit)	Value	Flag name	Description
OBJC_FLAGS	AND	0x4	FALSE	EDGE	Reject objects too close to the edge of the image
FLAGS	AND	0x10000000	TRUE	BINNED1	Accept only objects detected in the unbinned image
FLAGS	AND	0x20	FALSE	PEAKCENTER	Reject objects where the given centre is the position of the peak pixel, rather than based on the maximum likelihood estimator
FLAGS	AND	0x80	FALSE	NOPROFILE	Reject objects that are too small or too close to the edge to estimate a radial profile
FLAGS	AND	0x40000	FALSE	SATUR	Reject objects with one or more saturated pixels
FLAGS	AND	0x80000	FALSE	NOTCHECKED	Reject objects with pixels that were not checked to see whether they included a local peak, such as the cores of saturated stars
FLAGS	AND	0x400000	FALSE	BADSKY	Reject objects with a sky level so badly determined that the highest pixel in an object is *very* negative, far more so than a mere non-detection
FLAGS2	AND	0x100	FALSE	BAD_COUNTS_ERROR	Reject objects containing interpolated pixels that have too few good pixels to form a reliable estimate of the flux error
FLAGS2	AND	0x800	FALSE	SATUR_CENTER	Reject objects with a centre close to at least one saturated pixel
FLAGS2	AND	0x1000	FALSE	INTERP_CENTER	Reject objects with a centre close to at least one interpolated pixel
FLAGS2	AND	0x4000	FALSE	DEBLEND_NOPEAK	Reject child objects with no detected peak
FLAGS2	AND	0x8000	FALSE	PSF_FLUX_INTERP	Reject objects with more than 20 per cent of the PSF flux from interpolated pixels
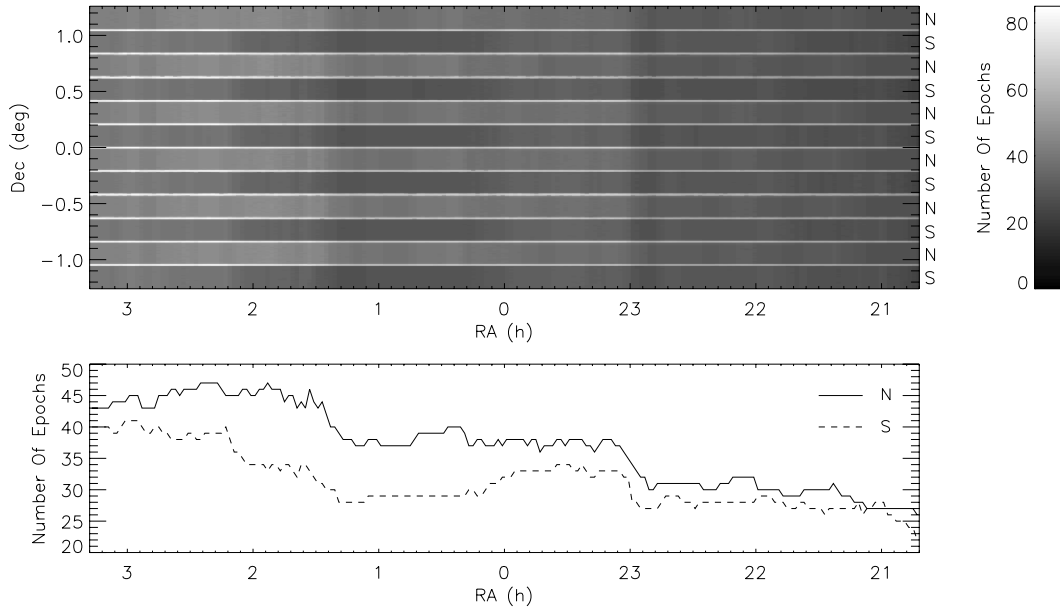
Figure 2. Top panel: Grey-scale image showing the maximum number of epochs in the light-motion curves as a function of object position. Bottom panel: Maximum number of epochs in the light-motion curves as a function of RA for a $0°.01$ wide slice through the grey-scale image centred at $\delta = -0°.1$ (continuous line: slice through the north strip) and for a similar slice centred at $\delta = 0°.1$ (dashed line: slice through the south strip).

methods depending on the number of epochs in the corresponding light-motion curve. If an object has a light-motion curve with six epochs or less, then the mean position is used for the expected position. Otherwise a mean position and proper motion are fitted to the light-motion curve and used to calculate the expected position of the object at the epoch of the current object record.

(iii) From the expected positions of the subset of objects, we find the closest object to the position of the current object record.[2] If the closest object lies within 0.7 arcsec, then the current object record is appended to the light-motion curve of the closest object, otherwise a new light-motion curve is created containing only the current object record.

Since each run contains at most one measurement of any object, the above algorithm can be performed in parallel for all objects from one run.

We choose to include both the PSF magnitude and exponential-profile magnitude (Stoughton et al. 2002) in a light-motion curve as a measure of an object's brightness in each waveband at each epoch. The PSF magnitude is the optimal measure of the brightness of a point-source object, and hence it is suitable for studying stars and quasars. Photometry of extended objects, such as galaxies, may be performed in a variety of ways, including fitting an exponential profile to the object image. The advantage of including the exponential magnitude as opposed to any of the other available profile magnitudes is that the difference between the PSF and exponential magnitudes, referred to as a concentration index, may be used as a continuous object-type classifier (Scranton et al. 2002), independent of the more restrictive binary SDSS classification.

After processing all Stripe 82 data, the LMCC was trimmed to only those objects that have a mean position in the range $\alpha = 20^h.7$ to $3^h.3$ and $\delta = -1°.26$ to $1°.26$. This was desirable because the tem-

poral coverage is too sparse outside these limits. The total area of sky covered by the LMCC is therefore ~ 249 deg^2. The LMCC was also searched for photometric outliers using a 3σ-clip algorithm for outlier identification, and we found clear groups of outliers clustered at specific HJDs. The tight clustering in time indicates that these groups of outliers are simply due to bad epochs (and not due to some astrophysical process, like an eclipse or flare), and hence we removed the corresponding data points, which amounted to ~ 1 per cent of all epochs.

In the top panel of Fig. 2, we plot a grey-scale image showing the maximum number of epochs in the light-motion curves as a function of object position. One may clearly see that the light-motion curves for objects in the overlap regions between the north and south strips contain approximately twice as many epochs as the light-motion curves for objects elsewhere. In the bottom panel, we plot a one-dimensional slice through the grey-scale image for $\delta = -0°.1$ and $\delta = 0°.1$ to further illustrate the dependence of the number of light-motion curve epochs on RA.

In Fig. 3, we plot sample photometric rms diagrams for the r band. The left-hand panel shows the rms PSF magnitude deviation versus mean PSF magnitude for 10 000 random PSF-like objects (MEAN_OBJECT_TYPE = 6; see Section 3.1) that have light-motion curves with at least 20 good r magnitude measurements. PSF-like objects are mainly stars with some contamination by quasars. Similarly, the right-hand panel shows the rms exponential magnitude deviation versus mean exponential magnitude for 10 000 random non-PSF-like objects (MEAN_OBJECT_TYPE = 3) that have light-motion curves with at least 20 good r magnitude measurements. Non-PSF-like objects are mainly galaxies.

Overplotted on each rms diagram is an empirical fit to the data using an exponential function of the form $f(m) = A + B\exp[C(m - 18)]$ where m denotes magnitude and A, B and C are fitted parameters (whose values are reported in the caption of Fig. 3). The fitting was done using an iterative 3σ-clip algorithm (see Vidrih index under Section 3.1). It is clear from these diagrams that for the r band we are achieving ~ 20 and 30 mmag rms accuracy

---

[2] Note that an object record contains a single datum for the celestial coordinates, calculated from the astrometric solution for the SDSS CCD camera at the current epoch.
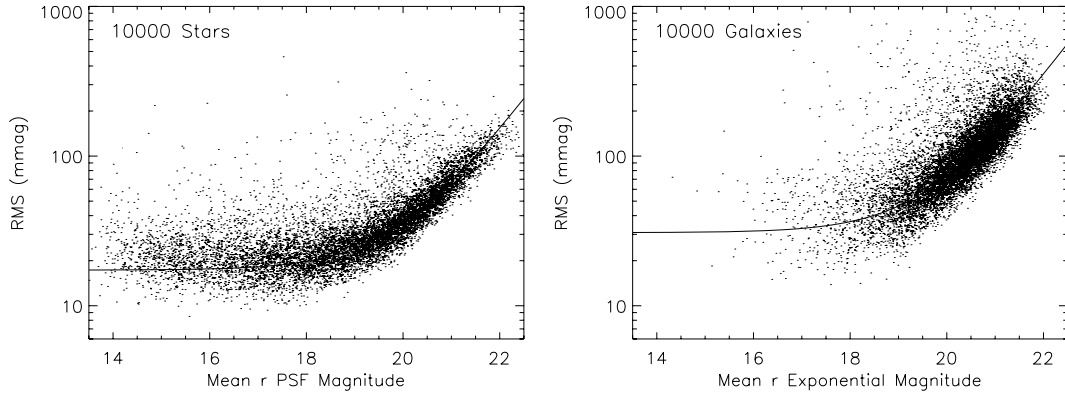
Figure 3. Left-hand panel: Plot of rms PSF magnitude deviation versus mean PSF magnitude for 10 000 random PSF-like objects (stars) with at least 20 good *r* magnitude measurements. Right-hand panel: Plot of rms exponential magnitude deviation versus mean exponential magnitude for 10 000 random non-PSF-like objects (galaxies) with at least 20 good *r* magnitude measurements. Both panels: Plotted functions (continuous lines) are all of the form $f(m) = A + B \exp[C(m - 18)]$ where m denotes magnitude and A, B and C are fitted parameters. For the left-hand panel, A, B and C have values 17.3, 2.48 mmag and 1.00, respectively. For the right-hand panel, A, B and C have values 30.8, 5.67 mmag and 1.01, respectively.

at $r \sim 18$ mag for PSF-like and non-PSF-like objects, respectively.[3] The rms diagrams for the other wavebands are very similar except for the *u* band, where we achieve ~ 23 and 50 mmag rms accuracy at $r \sim 18$ mag for PSF-like and non-PSF-like objects, respectively.

2.4 Further astrometric calibrations

Each SDSS imaging run was astrometrically calibrated against the US Naval Observatory CCD Astrograph Catalogue (UCAC; Zacharias et al. 2000), yielding absolute positions accurate to ~ 45 mas rms per coordinate (Pier et al. 2003). The accuracy is limited primarily by the accuracy of the UCAC positions (~ 70 mas rms at the UCAC survey limit of $R \simeq 16$), as well as the density of UCAC sources. The version of UCAC used to calibrate SDSS lacked proper motions, thus any proper motions based on SDSS positions will be systematically in error by the mean proper motion of the UCAC calibrators.

We illustrate the systematic errors inherent in the SDSS astrometry by considering galaxies in the magnitude range $17 < r < 19.5$ that have light-motion curves with at least 20 astrometric measurements. For this set of galaxies we measure the proper motion in RA and Dec., and we find that the galaxies are systematically moving with proper motions of the order of 10 mas per year in both RA and Dec.! The problem is clearly evident in Fig. 4(a) where we show histograms of the galaxy proper motions in RA (top left-hand panel) and Dec. (top right-hand panel). The trends of galaxy proper motion with RA are shown in the bottom left-hand panel for proper motion in RA and in the bottom right-hand panel for proper motion in Dec.

Proper motions based on multi-epoch SDSS data can be improved by recalibrating each SDSS imaging run against a reference SDSS run, rather than using the UCAC catalogue positions. The accuracy of the relative astrometry between runs is ~ 20 mas rms per coordinate (Pier et al. 2003), far superior to the accuracy of the absolute positions, due both to the more accurate centroids, as well as
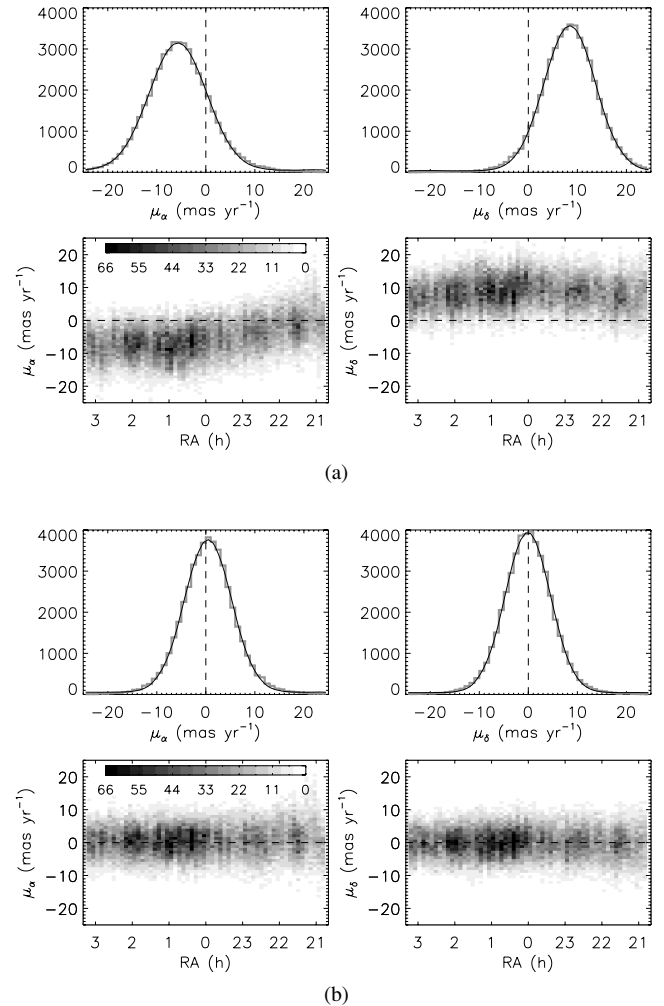
[3] The upturn in the rms amplitude for stars brighter than $r \sim 16$ is due to a combination of factors including: the appearance of detectable asymmetric low surface brightness structure (e.g. diffraction spikes) in the images; the effect of the large angular size of the images on the determination of the sky background.
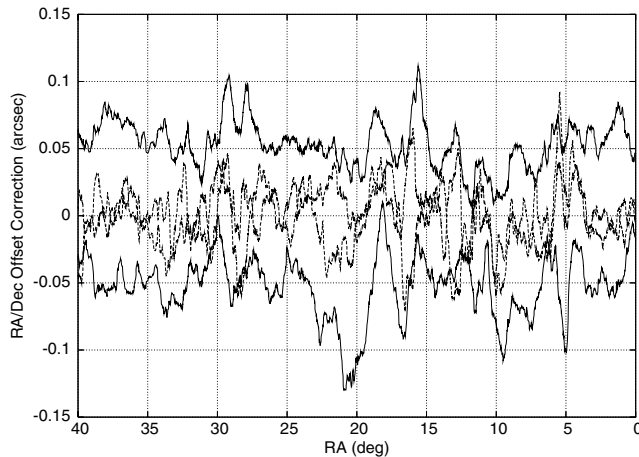

Figure 4. (a) Top row: Histograms of galaxy proper motions in RA (left-hand panel) and Dec. (right-hand panel) *before* astrometric recalibration. Bottom row: Density plots of galaxy proper motions in RA (left-hand panel) and Dec. (right-hand panel) as a function of RA *before* astrometric recalibration. The intensity bar has units of number of galaxies deg^{-1} mas^{-1} yr. (b) The same as Fig. 4(a) but *after* astrometric recalibration.

Figure 5. Plot of the mean offsets in RA and Dec. relative to the reference run 5823 as a function of RA for runs 94 (solid lines) and 5918 (dashed lines). For both runs we show the offsets for camera column 1, and for run 94, the lower and upper lines correspond to the RA and Dec. offsets, respectively. Note that this is but a small section of the full stripe.

the far greater density of calibrators, for SDSS compared to UCAC. Further, by using galaxies as calibrators, the proper motions can be tied to an extragalactic reference frame and are thus inertial. This is the method used in this paper to correct the systematic SDSS astrometric errors illustrated in Fig. 4(a). However, it is appropriate to mention that the positional system of the calibrators still refers to the epochs given by UCAC.

All imaging runs along the north strip have been recalibrated using run 5823 as the reference run. All imaging runs along the south strip have been recalibrated against run 4203, after first recalibrating run 4203 against run 5823. In order to recalibrate a target run, offsets in RA and Dec. are calculated for matching 'clean' galaxies in the reference run (rejecting galaxies affected by problems with deblending, pixel interpolation, multiple matches, etc. in either run). Only galaxies in the magnitude range $17 < r < 19.5$ are used to avoid large galaxies with poorly defined centroids. For each object in the target run, the mean offsets in RA and Dec. for the nearest[4] 100 such galaxies are calculated and added to the object position. This procedure recalibrates the positions in the target run to the reference frame defined by the galaxies in the reference run.

In Fig. 5, we show example mean offsets in RA and Dec. for camera column 1 from runs 94 and 5918. Note that run 94, observed in 1998, requires larger mean offsets to correct for the mean proper motion of the UCAC calibration stars than run 5918, observed in 2005, since it is further away in time from when the reference run 5823 was observed in 2005.

After recalibrating the astrometry for all light-motion curves in the LMCC, we have recreated Fig. 4(a) as Fig. 4(b) using the same sample of galaxies. The histograms of the galaxy proper motions in RA and Dec. are now centred around ∼0 mas yr^{-1} indicating that galaxies are stationary in the recalibrated astrometric system of the LMCC. Also, the lower panels demonstrate that the RA dependence of the galaxy proper motions has been properly removed.

There is also some evidence that the galaxy proper motion scatter has been improved. The rms deviation of the residuals about a fourth-

---

[4] Nearest in coordinate parallel to the scan direction, RA – the coordinate perpendicular to the scan direction, Dec., is ignored, as the length of the binning window is always larger than the width of a scan.

degree polynomial fit in each of the bottom panels of Fig. 4(a) is 5.4 mas yr^{-1} for RA and 5.2 mas yr^{-1} for Dec. This may be compared to the improved rms deviation of the proper motions in each of the bottom panels of Fig. 4(b) at 4.8 mas yr^{-1} for RA and 4.6 mas yr^{-1} for Dec.

The SDSS pipelines do not supply uncertainties on the measured celestial coordinates in the tsObj files, and so we have determined a noise model describing how the astrometric noise behaves as a function of magnitude. This was done by examining the distribution of coordinate rms for objects in the LMCC. However, we found that the astrometric noise in the 2005 observing season was noticeably larger than in previous seasons, most likely due to the less stringent restrictions on observing conditions leading to a greater spread in PSF full width at half-maximum (FWHM) and object signal-to-noise ratio. To properly account for this, we determined separate noise models for the pre-2005 and 2005 observing seasons.

To determine the astrometric noise models, we select all PSF-like objects (MEAN_OBJECT_TYPE = 6) with at least 20 good epochs in r in each of the pre-2005 and 2005 observing seasons. For these objects we derive the distribution of coordinate rms deviations for 0.5-mag bins for both pre-2005 and 2005 data, and fit a peak and dispersion for each bin. In Fig. 6(a), we plot the peak RA rms deviation for each magnitude bin versus r magnitude for pre-2005 data (filled circles) and 2005 data (open circles; offset by 0.15 mag to the left-hand side for clarity). We obtain very similar results for the Dec. coordinate. We fit the peak data as a function of magnitude m via an exponential function of the form $f(m) = A + B \exp[C(m - 18)]$ where A, B and C are fitted parameters, and plot the fitted models in Fig. 6(a) as continuous and dashed curves for pre-2005 and 2005 data, respectively.

The following equations represent our final adopted astrometric noise model, based on the exponential model fits for both the RA and Dec. coordinates:

$$\text{Pre-2005:}\ \sigma_\alpha(t) = \sigma_\delta(t) = 32.0 + 0.430 \exp\{1.34\,[m(t) - 18]\}\,,$$
$$\text{2005:}\ \sigma_\alpha(t) = \sigma_\delta(t) = 35.4 + 0.783 \exp\{1.09\,[m(t) - 18]\}\,,$$
$$(1)$$

where $\sigma_\alpha(t)$ and $\sigma_\delta(t)$ are the uncertainties on the measured celestial coordinates $\alpha(t)$ and $\delta(t)$, respectively, at time t, and $m(t)$ represents the brightest PSF magnitude out of the five photometric measurements at time t. Evidence that this noise model is valid comes from the fact that the distribution of χ^2 per degree of freedom of the proper motion fit for the HLC (Section 3.1) is peaked at a value of ∼1.1. Note that astrometric uncertainties are not given in the LMCC and should be obtained via equation (1).

In Fig. 6(b), we plot the results of the same coordinate rms deviation analysis for non-PSF-like objects (MEAN_OBJECT_TYPE = 3) with at least 20 good epochs in r in each of the pre-2005 and 2005 observing seasons. It is clear from the plots in Fig. 6 that we are achieving ∼32 and 35 mas rms accuracy at $r \sim 18$ mag for stars for pre-2005 and 2005 data, respectively, and ∼35 and 46 mas rms accuracy at $r \sim 18$ mag for galaxies for pre-2005 and 2005 data, respectively.

2.5 Catalogue format

The LMCC exists as eight tar files, one for each hour in RA from 20^h to 4^h. Each tar file contains 60 subdirectories corresponding to the minutes of RA, and the light-motion curves are stored in these directories based on their mean RA coordinates. The LMCC contains 3700 548 light-motion curves, 2807 047 of which have at least 20 epochs. The tar files (∼29.5 GB compressed) may be obtained
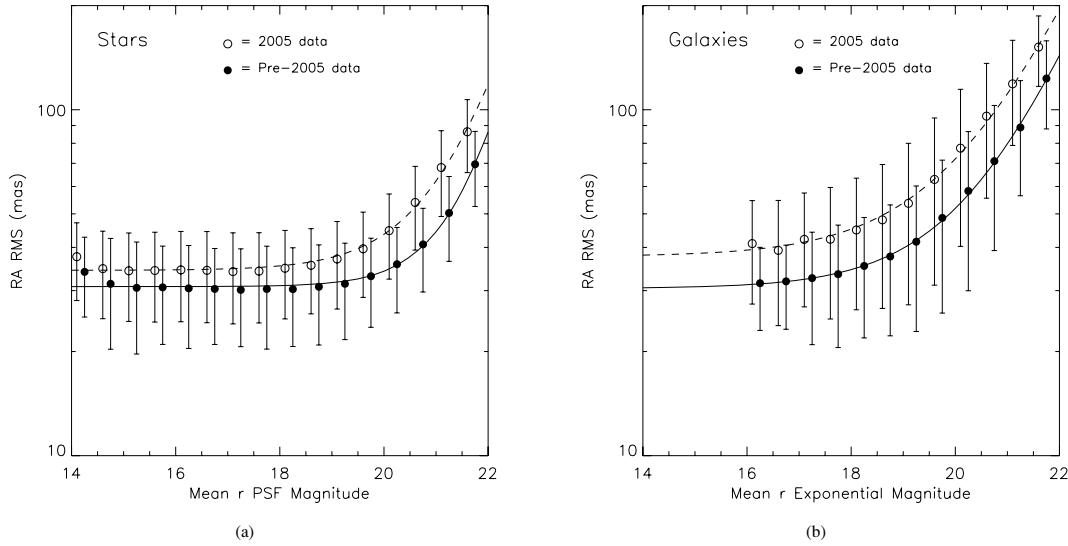
Figure 6. (a) Plot of the peak RA rms deviation in 0.5-mag bins versus *r* magnitude for PSF-like objects (stars) for pre-2005 data (filled circles) and 2005 data (open circles; offset by 0.15 mag to the left-hand side for clarity). (b) Plot of the peak RA rms deviation in 0.5-mag bins versus *r* magnitude for non-PSF-like objects (galaxies) for pre-2005 data (filled circles) and 2005 data (open circles; offset by 0.15 mag to the left-hand side for clarity). Both panels: Error bars represent the dispersion in the distribution of rms deviations in each magnitude bin. Plotted functions (continuous and dashed curves) are all of the form $f(m) = A + B \exp[C(m - 18)]$ where *m* denotes magnitude and *A*, *B* and *C* are fitted parameters.

by web download from http://das.sdss.org/value_added/stripe_82_variability/SDSS_82_public/. Light-motion curve plotting tools written in IDL may also be downloaded from the same web site.

A single light-motion curve is stored as an ASCII file with a name constructed from the unweighted mean position of the corresponding object. The ASCII light-motion curve file contains a header line describing the column meanings, followed by exactly five rows for each epoch (one row for each waveband) in strict time order. All five waveband measurements are included for completeness, even though it is possible that at any one epoch, up to four waveband measurements may not satisfy the quality criteria described in Section 2.3. In Table 3 we describe the columns that make up a light-motion curve from the LMCC.

Fig. 7 shows some clear examples of photometric variability and motion from the LMCC. Fig. 7(a) presents the light curve in *r* (upper points) and *g* (lower points) of the large-amplitude long-period variable star SDSS J220514.58+000845.7, most likely a Mira variable (Watkins et al., in preparation). Fig. 7(b) presents the motion curve of the known ultracool white dwarf SDSS J224206.19+004822.7 (Kilić et al. 2006). Both panels illustrate the dramatic increase in temporal sampling produced by the start of the SDSS-II Supernova Survey in 2005.

3 THE HIGHER LEVEL CATALOGUE

3.1 Catalogue description

The HLC supplies a set of 229 derived quantities for each light-motion curve in the LMCC. These quantities are aimed at describing the mean magnitudes, photometric variability and astrometric motion of the objects in the LMCC, and they are calculated using only light-motion curve entries that satisfy the quality constraints from Section 2.3. Those quantities in the HLC related to photometry are described in Table 4, while those related to astrometry are described in Table 5.

In Table 4, if a tag name is associated with a five-element array, then the five values represent the described quantity for each

of the five SDSS wavebands in the order *u*, *g*, *r*, *i* and *z*. When a certain waveband has insufficient 'good' light-motion curve entries to calculate a particular quantity, a value of zero is stored (this also applies to Table 5). For instance, the first value in the array MEAN_PSFMAG is set to zero for any light-motion curves with no 'good' entries for the *u* band.

All quantities in Table 4 with CLIP at the end of the tag name are calculated using a 4σ-clip algorithm that rejects only the worst outlier at any one iteration, and terminates when no more outliers are identified. Similarly, all quantities in Table 4 with ITER at the end of the tag name are calculated using the iterative procedure described in Stetson (1996) to dynamically reweight data points based on the size of the residuals from the mean. Both these sets of quantities have been designed to be more robust against outliers than a simple inverse variance weighted mean.

The SDSS photometric pipeline performs a morphological star/galaxy separation, the quality of which is intimately related to seeing and sky brightness. While the accuracy is very good for bright objects, there can be confusion for faint objects. The quantity MEAN_OBJECT_TYPE in Table 4 is an unweighted mean of the SDSS object type classification. Hence it has a value of 3 if the object is classified as a galaxy at all epochs, a value of 6 if the object is classified as a star at all epochs, and a value between 3 and 6 otherwise. The reliability of MEAN_OBJECT_TYPE for object type classification depends on the reliability of the SDSS object type classifier and the number of epochs at which the object was observed.

The quantity MEAN_CHILD in Table 4 is an unweighted mean of whether the child object bit is set or not. In other words, this quantity has a value of 1 if, at all epochs, the object results from the deblending of a parent object, a value of 0 if the object was never the result of the deblending of a parent object, and a value between 0 and 1 otherwise.

The Galactic extinctions described by EXTINCTION in Table 4 are derived using the maps of dust column density from Schlegel, Finkbeiner & Davis (1998).

For eclipse and flare detection in light curves we include the statistics ECL_STAT and FLARE_STAT (Table 4) in the HLC. In

Table 3. The list of columns that make up a light-motion curve in the LMCC along with a brief description.

Column number	Column name	Type	Description
1	Run	INTEGER	SDSS imaging run
2	Rerun	INTEGER	Version of the SDSS FRAMES pipeline used to process the data
3	Field	INTEGER	SDSS field number along a strip
4	Camcol	INTEGER	SDSS camera column
5	Filter	INTEGER	SDSS waveband ($0 = u, 1 = g, 2 = r, 3 = i, 4 = z$)
6	Object type	INTEGER	Object classification ($3 =$ galaxy, $6 =$ star)
7	RA	DOUBLE	RA J2000 (°)
8	Dec.	DOUBLE	Dec. J2000 (°)
9	Row	FLOAT	CCD row coordinate (pix)
10	Column	FLOAT	CCD column coordinate (pix)
11	HJD	DOUBLE	Heliocentric Julian Date (d)
12	PSF luptitude	FLOAT	PSF magnitude (lup)[a]
13	PSF luptitude error	FLOAT	Uncertainty on the PSF magnitude (lup)[a]
14	PSF flux	FLOAT	PSF flux normalized by the flux from a zeroth magnitude object
15	PSF flux error	FLOAT	Uncertainty on the PSF flux
16	Exp luptitude	FLOAT	Exponential magnitude (lup)[a]
17	Exp luptitude error	FLOAT	Uncertainty on the exponential magnitude (lup)[a]
18	Exp flux	FLOAT	Exponential flux normalized by the flux from a zeroth magnitude object
19	Exp flux error	FLOAT	Uncertainty on the exponential flux
20	Sky	FLOAT	Sky background brightness (lup arcsec^{-2})[a]
21	Sky error	FLOAT	Uncertainty on the sky background brightness (lup arcsec^{-2})[a]
22	FWHM	FLOAT	FWHM of the PSF (arcsec)
23	Photometric calibration tag	INTEGER	Flag indicating the photometric calibration status (1 = calibrated, 0 = uncalibrated)
24	Photometric zero-point	FLOAT	Fractional flux offset applied to the flux values
25	Flag 1	LONG	Object flags (tsObj file tag FLAGS)
26	Flag 2	LONG	More object flags (tsObj file tag FLAGS2)
27	Astrometric calibration tag	INTEGER	Flag indicating the astrometric calibration status (1 = calibrated, 0 = uncalibrated)
28	RA correction	DOUBLE	Correction applied to RA (°)
29	Dec. correction	DOUBLE	Correction applied to Dec. (°)

[a]See Lupton et al. (1999) and Stoughton et al. (2002) for the definition of a luptitude.

calculating these values, we assume that any eclipse/flare event in a light curve will include only one photometric data point since the time elapsed between consecutive scans is at least one day. Hence, for each photometric data point (using PSF magnitudes only), we calculate the statistic S^2, based on a matched filter from Bramich et al. (2005), and defined by

$$S^2 \equiv \frac{\chi^2_{\text{const}} - \chi^2_{\text{out}}}{\left(\chi^2_{\text{out}}/\nu\right)}, \qquad (2)$$

where χ^2_{const} is the χ^2 value of a constant fit for each waveband to the whole light curve, and χ^2_{out} and ν are the χ^2 and number of degrees freedom, respectively, of a constant fit for each waveband to the out-of-eclipse/flare light curve. In order to avoid false positives, we only calculate S^2 for epochs with photometric data points that are 'good' in at least two wavebands. The adopted values of ECL_STAT and FLARE_STAT are then taken to be the largest values of S^2 for photometric data points fainter and brighter, respectively, than the mean. We also record the corresponding values of χ^2_{out}/ν for ECL_STAT and FLARE_STAT in the quantities ECL_REDCHISQ_OUT and FLARE_REDCHISQ_OUT, respectively, along with the epoch of the putative eclipse/flare event in ECL_EPOCH and FLARE_EPOCH, respectively.

In Table 4, the Stetson variability indices J, K and L (Stetson 1996) for both the PSF and exponential magnitudes are stored in the quantities with tag names starting STETSON_INDEX. We chose the r band as the comparison waveband and consequently the third element in each of these six quantity arrays is set to zero.

Our final measure of light curve variability is via a quantity called the Vidrih variability index. Rms magnitude devia-

tions for non-variable light curves plotted versus mean magnitude m in a given waveband (referred to as an rms diagram) are scattered around a three parameter empirical exponential function $f(m) = A + B \exp[C(m - 18)]$, while the rms magnitude deviation of variable sources is expected to be noticeably larger. We consider two light-curve samples, that of PSF-like objects (MEAN_OBJECT_TYPE = 6) and non-PSF-like objects (MEAN_OBJECT_TYPE = 3). For each light-curve sample and waveband, we iteratively fitted $f(m)$ to the corresponding rms diagrams using a 3σ-clip algorithm, employing PSF magnitudes for the star light-curve sample and exponential magnitudes for the galaxy light-curve sample. In each case we also constructed a function $g(m)$ describing the standard deviation of the scatter around $f(m)$ via a four-degree polynomial fit to the standard deviation of the rms magnitude deviations measured in 0.25-mag bins. Then, for any light curve, the Vidrih index V was calculated as its rms magnitude deviation minus $f(m)$, normalized by $g(m)$, with negative values set to zero, and it is stored in the quantities with tag names starting VIDRIH_INDEX (Table 4). Note that due to the way the Vidrih indices are constructed, VIDRIH_INDEX_PSF is only relevant to stars and VIDRIH_INDEX_EXP is only relevant to galaxies.

In Table 5, we describe the quantities associated with the object astrometry. Specifically we fit a proper motion model for celestial coordinates (α, δ), in degrees, at Heliocentric Julian Date t, in days, for each light-motion curve:

$$\alpha(t) = \text{RA\_MEAN} + \frac{7.605 \times 10^{-7} \text{RA\_PM}}{\cos(\text{DEC\_MEAN})} (t - \text{T0}), \qquad (3)$$

$$\delta(t) = \text{DEC\_MEAN} + 7.605 \times 10^{-7} \text{DEC\_PM} (t - \text{T0}). \qquad (4)$$
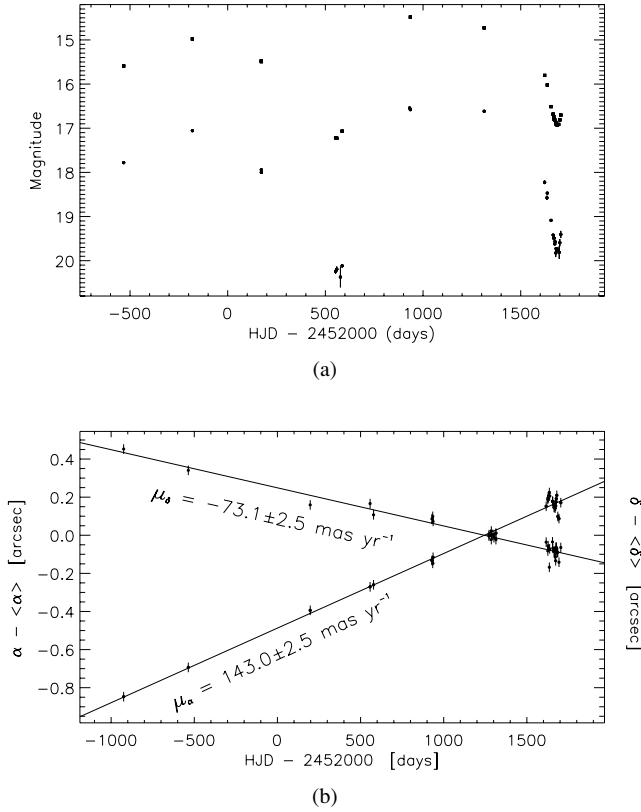
(a)

(b)

Figure 7. (a) Light curve of the Mira variable star candidate SDSS J220514.58+000845.7 in the *r* (upper points) and *g* (lower points) bands. (b) Fitted proper motion in RA (track at bottom left-hand side, left-hand *y*-axis) and Dec. (track at top left-hand side, right-hand *y*-axis) for the ultracool white dwarf SDSS J224206.19+004822.7 (Kilić et al. 2006).

We set T0 as the weighted mean of the epochs of observation:

$$\mathrm{T0} = \frac{\sum_j t_j/\sigma_\alpha(t_j)^2}{\sum_j 1/\sigma_\alpha(t_j)^2}, \tag{5}$$

where t_i represents the set of Heliocentric Julian Dates for the positional measurements, and $\sigma_\alpha(t_i)$ represents the set of uncertainties on the measured celestial coordinates α_i and δ_i. The uncertainties $\sigma_\alpha(t_i)$ are calculated via equation (1).

We solve for the quantities RA_MEAN, RA_PM, DEC_MEAN and DEC_PM by minimizing the appropriate χ^2 using a downhill simplex algorithm. We calculate the uncertainties on these quantities, namely RA_MEAN_ERR, RA_PM_ERR, DEC_MEAN_ERR and DEC_PM_ERR, by assuming that $\cos(\mathrm{DEC\_MEAN}) \approx 1$ (a valid assumption for $|\delta| \leqslant 1°26$) and noting that minimizing the χ^2 for each of the resulting equations is a linear least-squares problem with an analytic solution. We supply the best-fitting χ^2 values via the quantities RA_CHISQ_LIN and DEC_CHISQ_LIN, and we record the number of positional measurements used in the fit in the quantity N_POS_EPOCHS. We also supply the χ^2 values RA_CHISQ_CON and DEC_CHISQ_CON for a model including only a mean position, which facilitates the calculation of the following $\Delta\chi^2$:

$$\Delta\chi^2_\mu = \mathrm{RA\_CHISQ\_CON} - \mathrm{RA\_CHISQ\_LIN} \\ + \mathrm{DEC\_CHISQ\_CON} - \mathrm{DEC\_CHISQ\_LIN}. \tag{6}$$

The statistic $\Delta\chi^2_\mu$ may be used to calculate the significance of a proper motion measurement by noting that it follows a χ^2 distribution with two degrees of freedom.

The whole fitting process is also iterated using a clipping algorithm that rejects the worst outlier at any one iteration, and terminates when the change in the fitted proper motion is smaller than 3 mas yr^{-1}. Consequently, all the derived astrometric quantities described so far have a corresponding quantity calculated for the clipped positional measurements and stored in the HLC (all quantities listed in Table 5 with a tag name ending CLIP). The astrometric quantities derived from the clipped astrometric data are more robust than those derived from the unclipped astrometric data. We strongly advise that any statistical studies undertaken with the astrometry in the HLC should only use the clipped quantities.

Finally, we have attempted to detect the parallax signal for nearby stars by fitting a parallax model to each light-motion curve. However, our investigation has made it clear that the distribution of observations during the same few months each year along with the positional accuracy of the astrometric measurements are not enough to enable the detection of a clean parallax signal.

3.2 Catalogue format

The HLC is stored in eight FITS binary tables, one for each hour in RA from 20^h to 4^h. Each record in the HLC corresponds to a single light-motion curve and stores 229 derived quantities with tag names listed and described in Tables 4 and 5. The FITS files ($\sim$1.9 GB compressed) may be obtained by web download from http://das.sdss.org/value_added/stripe_82_variability/SDSS_82_public/.

The IDL Astronomy User's Library[5] function 'mrdfits' is a convenient way to read in the HLC, storing the FITS binary table automatically in an IDL structure. The IDL 'where' function then becomes a very powerful tool for accessing subsets of data with ease.

4 EXTERNAL COMPARISONS

4.1 Photometry

The most relevant comparison of our catalogue photometry can be made by comparing our results to those of Ivezić et al. (2007) (hereafter IV07) who use 58 pre-2005 SDSS-I imaging runs of Stripe 82, observed under mostly photometric conditions, to construct a standard star catalogue. IV07 match unsaturated point sources satisfying high signal-to-noise ratio criteria (photometric uncertainties below 0.05 mag) between runs and choose sources with at least four epochs. Those objects that are identified as non-varying, by requiring a χ^2 per degree of freedom for the mean magnitudes of less than 3 in the *g*, *r* and *i* bands, are chosen as candidate standard stars. The standard star catalogue is then internally recalibrated, correcting for flat-field errors and time-variable extinction (e.g. due to clouds).

The main differences between the LMCC and the IV07 catalogue are that we use a different photometric recalibration method, but based on the same idea of spatially dependent photometric zero-points, and that we include the generally non-photometric observations from the SDSS-II supernova runs. Not surprisingly, for the 886 396 objects from the IV07 catalogue in the overlap area with the LMCC, we find unambiguous matches in the LMCC for 886 191 objects using a match radius of 0.7 arcsec, where the missing fraction of $\sim$0.02 per cent can be explained by the different criteria

---

[5] The IDL Astronomy User's Library is web-hosted at http://idlastro.gsfc.nasa.gov/ and maintained by Wayne Landsman at the Goddard Space Flight Centre.

Table 4. The list of derived quantities related to photometry that are stored for each light-motion curve in the HLC. These quantities are calculated using only light-motion curve entries that satisfy the quality constraints from Section 2.3.

Tag name in HLC	Type	Description
LC_NAME	STRING	Light-motion curve filename
IAU_NAME	STRING	Object name in SDSS Data Release 6 (International Astronomical Union approved format)[a]
N_GOOD_EPOCHS	5 × INTEGER	Number of good photometric data points
MEAN_PSFMAG	5 × FLOAT	Inverse variance weighted mean of the PSF magnitudes
MEAN_PSFMAG_ERR	5 × FLOAT	Uncertainty on MEAN_PSFMAG
MEAN_EXPMAG	5 × FLOAT	Inverse variance weighted mean of the exponential magnitudes
MEAN_EXPMAG_ERR	5 × FLOAT	Uncertainty on MEAN_EXPMAG
RMS_PSFMAG	5 × FLOAT	Rms deviation of the PSF magnitudes
RMS_EXPMAG	5 × FLOAT	Rms deviation of the exponential magnitudes
CHISQ_PSFMAG	5 × FLOAT	χ^2 of the PSF magnitudes
CHISQ_EXPMAG	5 × FLOAT	χ^2 of the exponential magnitudes
N_GOOD_EPOCHS_PSF_CLIP	5 × INTEGER	Number of good PSF magnitudes after 4σ-clipping[b]
N_GOOD_EPOCHS_EXP_CLIP	5 × INTEGER	Number of good exponential magnitudes after 4σ-clipping[b]
MEAN_PSFMAG_CLIP	5 × FLOAT	4σ-clipped inverse variance weighted mean of the PSF magnitudes[b]
MEAN_PSFMAG_ERR_CLIP	5 × FLOAT	Uncertainty on MEAN_PSFMAG_CLIP[b]
MEAN_EXPMAG_CLIP	5 × FLOAT	4σ-clipped inverse variance weighted mean of the exponential magnitudes[b]
MEAN_EXPMAG_ERR_CLIP	5 × FLOAT	Uncertainty on MEAN_EXPMAG_CLIP[b]
RMS_PSFMAG_CLIP	5 × FLOAT	Rms deviation of the 4σ-clipped PSF magnitudes[b]
RMS_EXPMAG_CLIP	5 × FLOAT	Rms deviation of the 4σ-clipped exponential magnitudes[b]
CHISQ_PSFMAG_CLIP	5 × FLOAT	χ^2 of the 4σ-clipped PSF magnitudes[b]
CHISQ_EXPMAG_CLIP	5 × FLOAT	χ^2 of the 4σ-clipped exponential magnitudes[b]
MEAN_PSFMAG_ITER	5 × FLOAT	Iterated inverse variance weighted mean of the PSF magnitudes[b]
MEAN_PSFMAG_ERR_ITER	5 × FLOAT	Uncertainty on MEAN_PSFMAG_ITER[b]
MEAN_EXPMAG_ITER	5 × FLOAT	Iterated inverse variance weighted mean of the exponential magnitudes[b]
MEAN_EXPMAG_ERR_ITER	5 × FLOAT	Uncertainty on MEAN_EXPMAG_ITER[b]
PERCENTILE_05_PSF	5 × FLOAT	5th percentile of the cumulative distribution of PSF magnitudes
PERCENTILE_50_PSF	5 × FLOAT	Median of the PSF magnitudes
PERCENTILE_95_PSF	5 × FLOAT	95th percentile of the cumulative distribution of PSF magnitudes
PERCENTILE_05_EXP	5 × FLOAT	5th percentile of the cumulative distribution of exponential magnitudes
PERCENTILE_50_EXP	5 × FLOAT	Median of the exponential magnitudes
PERCENTILE_95_EXP	5 × FLOAT	95th percentile of the cumulative distribution of exponential magnitudes
TIME_SPAN	FLOAT	Time-span of the light-motion curve (d)
MEAN_OBJECT_TYPE	FLOAT	Unweighted mean of the object classification[b]
MEAN_CHILD	FLOAT	Unweighted mean of whether the child bit is set or not[b]
EXTINCTION	5 × FLOAT	Galactic extinction (mag)[b]
ECL_REDCHISQ_OUT	FLOAT	Reduced χ^2 out-of-eclipse for the PSF magnitudes[b]
ECL_STAT	FLOAT	Eclipse statistic for the PSF magnitudes[b]
ECL_EPOCH	DOUBLE	Eclipse epoch as a Heliocentric Julian Date (d)[b]
FLARE_REDCHISQ_OUT	FLOAT	Reduced χ^2 out-of-flare for the PSF magnitudes[b]
FLARE_STAT	FLOAT	Flare statistic for the PSF magnitudes[b]
FLARE_EPOCH	DOUBLE	Flare epoch as a Heliocentric Julian Date (d)[b]
STETSON_INDEX_J_PSF	5 × FLOAT	Stetson J index for the PSF magnitudes[b]
STETSON_INDEX_J_EXP	5 × FLOAT	Stetson J index for the exponential magnitudes[b]
STETSON_INDEX_K_PSF	5 × FLOAT	Stetson K index for the PSF magnitudes[b]
STETSON_INDEX_K_EXP	5 × FLOAT	Stetson K index for the exponential magnitudes[b]
STETSON_INDEX_L_PSF	5 × FLOAT	Stetson L index for the PSF magnitudes[b]
STETSON_INDEX_L_EXP	5 × FLOAT	Stetson L index for the exponential magnitudes[b]
VIDRIH_INDEX_PSF	5 × FLOAT	Vidrih index for the PSF magnitudes[b]
VIDRIH_INDEX_EXP	5 × FLOAT	Vidrih index for the exponential magnitudes[b]

[a]May be empty. [b]See text for more details.

used to construct the two catalogues. Of the 886 191 matching objects in the LMCC, 219 627, 606 658, 879 766, 886 028 and 856 456 objects have at least three good epochs in the u, g, r, i and z bands, respectively, and mean PSF magnitudes brighter than 21.5, 21.5, 21.5, 21.5 and 20.5 mag, respectively. It is these objects that we use when constructing the histograms in Fig. 8.

In Fig. 8, each row of panels corresponds to a different waveband and the order employed is u, g, r, i and z from the top row to the bottom row. The left-hand column of plots are normalized histograms of χ^2 per degree of freedom for the mean PSF magnitudes in the HLC,

and they serve to confirm that the photometric uncertainties in the LMCC (inherited from the SDSS pipelines, with some adjustment during photometric recalibration) are correct, since the histograms peak at a value of $\chi^2/(N-1) \sim 1$.

The middle column panels in Fig. 8 are normalized histograms of the uncertainties on the mean PSF magnitudes in the HLC (solid lines) and on the mean magnitudes from the IV07 catalogue (dashed lines). It is clear that the mean magnitudes quoted in the HLC are approximately twice as precise as those from IV07, which is due to the greater number of epochs included in the LMCC. However,

Table 5. The list of derived quantities related to astrometry that are stored for each light-motion curve in the HLC. These quantities are calculated using only light-motion curve entries that satisfy the quality constraints from Section 2.3.

Tag name in HLC	Type	Description
RA_MEAN	DOUBLE	Inverse variance weighted mean of the RA measurements ($°$)
RA_MEAN_ERR	FLOAT	Uncertainty on RA_MEAN ($°$)
RA_PM	FLOAT	Proper motion in the RA coordinate (arcsec yr^{-1})
RA_PM_ERR	FLOAT	Uncertainty on RA_PM (arcsec yr^{-1})
RA_CHISQ_CON	FLOAT	χ^2 of the RA measurements for a model that includes only a mean position
RA_CHISQ_LIN	FLOAT	χ^2 of the RA measurements for a model that includes a mean position and a proper motion
RA_MEAN_CLIP	DOUBLE	Inverse variance weighted mean of the clipped RA measurements ($°$)
RA_MEAN_ERR_CLIP	FLOAT	Uncertainty on RA_MEAN_CLIP ($°$)
RA_PM_CLIP	FLOAT	Proper motion in the RA coordinate for the clipped RA measurements (arcsec yr^{-1})
RA_PM_ERR_CLIP	FLOAT	Uncertainty on RA_PM_CLIP (arcsec yr^{-1})
RA_CHISQ_CON_CLIP	FLOAT	χ^2 of the clipped RA measurements for a model that includes only a mean position
RA_CHISQ_LIN_CLIP	FLOAT	χ^2 of the clipped RA measurements for a model that includes a mean position and a proper motion
DEC_MEAN	DOUBLE	Inverse variance weighted mean of the Dec measurements ($°$)
DEC_MEAN_ERR	FLOAT	Uncertainty on DEC_MEAN ($°$)
DEC_PM	FLOAT	Proper motion in the Dec. coordinate (arcsec yr^{-1})
DEC_PM_ERR	FLOAT	Uncertainty on DEC_PM (arcsec yr^{-1})
DEC_CHISQ_CON	FLOAT	χ^2 of the Dec. measurements for a model that includes only a mean position
DEC_CHISQ_LIN	FLOAT	χ^2 of the Dec. measurements for a model that includes a mean position and a proper motion
DEC_MEAN_CLIP	DOUBLE	Inverse variance weighted mean of the clipped Dec. measurements ($°$)
DEC_MEAN_ERR_CLIP	FLOAT	Uncertainty on DEC_MEAN_CLIP ($°$)
DEC_PM_CLIP	FLOAT	Proper motion in the Dec. coordinate for the clipped Dec. measurements (arcsec yr^{-1})
DEC_PM_ERR_CLIP	FLOAT	Uncertainty on DEC_PM_CLIP (arcsec yr^{-1})
DEC_CHISQ_CON_CLIP	FLOAT	χ^2 of the clipped Dec. measurements for a model that includes only a mean position
DEC_CHISQ_LIN_CLIP	FLOAT	χ^2 of the clipped Dec. measurements for a model that includes a mean position and a proper motion
T0	DOUBLE	Inverse variance weighted mean of the Heliocentric Julian Dates using the uncertainties on the astrometric measurements (d)
T0_CLIP	DOUBLE	Inverse variance weighted mean of the Heliocentric Julian Dates for the clipped astrometric measurements (d)
N_POS_EPOCHS	INTEGER	Number of good positional measurements
N_POS_EPOCHS_CLIP	INTEGER	Number of good positional measurements after clipping

systematic errors are still likely to dominate the mean magnitudes at the ~1 per cent level, which corresponds to the level of the photometric recalibrations and to the systematic error introduced by the slightly different band passes of each column of detectors in the SDSS camera. We do not correct the LMCC magnitudes for the different bandpasses in contrast to IV07.

The right-hand column panels in Fig. 8 are normalized histograms of the difference between the HLC mean PSF magnitudes and the IV07 catalogue mean magnitudes. A Gaussian has been fitted to each histogram (dotted lines), and the fitted centre and sigma are quoted in each panel. The histograms are centred around zero at the millimagnitude level, except for the *u* band where the IV07 photometry is slightly offset from the HLC photometry by ~4 mmag. The histograms have σ values of 28, 13, 11, 10 and 16 mmag in u, g, r, i and z, respectively, which are consistent with the scatter in the photometric zero-points of the standard SDSS runs derived in Section 2.2, and with the scatter in the similar internal photometric recalibrations of IV07.

The data set used to construct the IV07 standard star catalogue is a subset of the data used to construct the LMCC, and therefore we can use our superior temporal coverage to identify standard star candidates that are actually photometrically variable. Watkins et al. (in preparation) use the HLC to systematically identify variable stars in Stripe 82, and we choose to follow all but one of their cuts on the HLC quantities. Of the 886 191 objects from the IV07 catalogue that have matching objects in the LMCC, 878 172 have at least 11 good epochs in the *g* band, allowing for the calculation of reliable variability and object type indicators. The requirement from Watkins et al. (in preparation) that an LMCC object has a mean

object type greater than 5.5 ensures that chosen variables are PSF-like (stars). However, this implies that 16 529 objects are probably non-PSF-like, corresponding to a fraction of ~1.9 per cent. Hence, we do not apply this requirement, and instead we directly apply the remaining requirements that a variable object should have a χ^2 per degree of freedom greater than 3 for both the *g*- and *r*-band mean PSF magnitudes, and a Stetson *L* index greater than 1 for the *g* band. We find that just 570 IV07 standard stars, from 878 172, are variable, corresponding to a fraction of ~0.065 per cent. This confirms that even with the addition of many more photometric data, the IV07 standard stars are in general still found to be constant at the ~0.01 mag level. In considering the full IV07 catalogue with 1 006 849 candidate standard stars, we suspect that ~650 are actually variables.

4.2 Astrometry

Gould & Kollmeier (2004) (hereafter GK04) carefully combine SDSS Data Release 1 (SDSS DR1) and USNO-B proper motions to produce a catalogue of 390 476 objects with proper motions $\mu \geqslant 20$ mas yr^{-1} and magnitudes $r \leqslant 20$ mag. SDSS DR1 proper motions are based on matches of SDSS to USNO-A2.0 (Monet et al. 1998), which suffer from mismatches causing spurious high proper motion objects, and systematic trends in proper motion. However, by cross-correlating SDSS DR1 and USNO-B, GK04 successfully removed the vast majority of spurious proper motion stars. Furthermore, by considering the set of spectroscopically confirmed quasars in SDSS DR1, GK04 calibrate out the position-dependent astrometric biases,
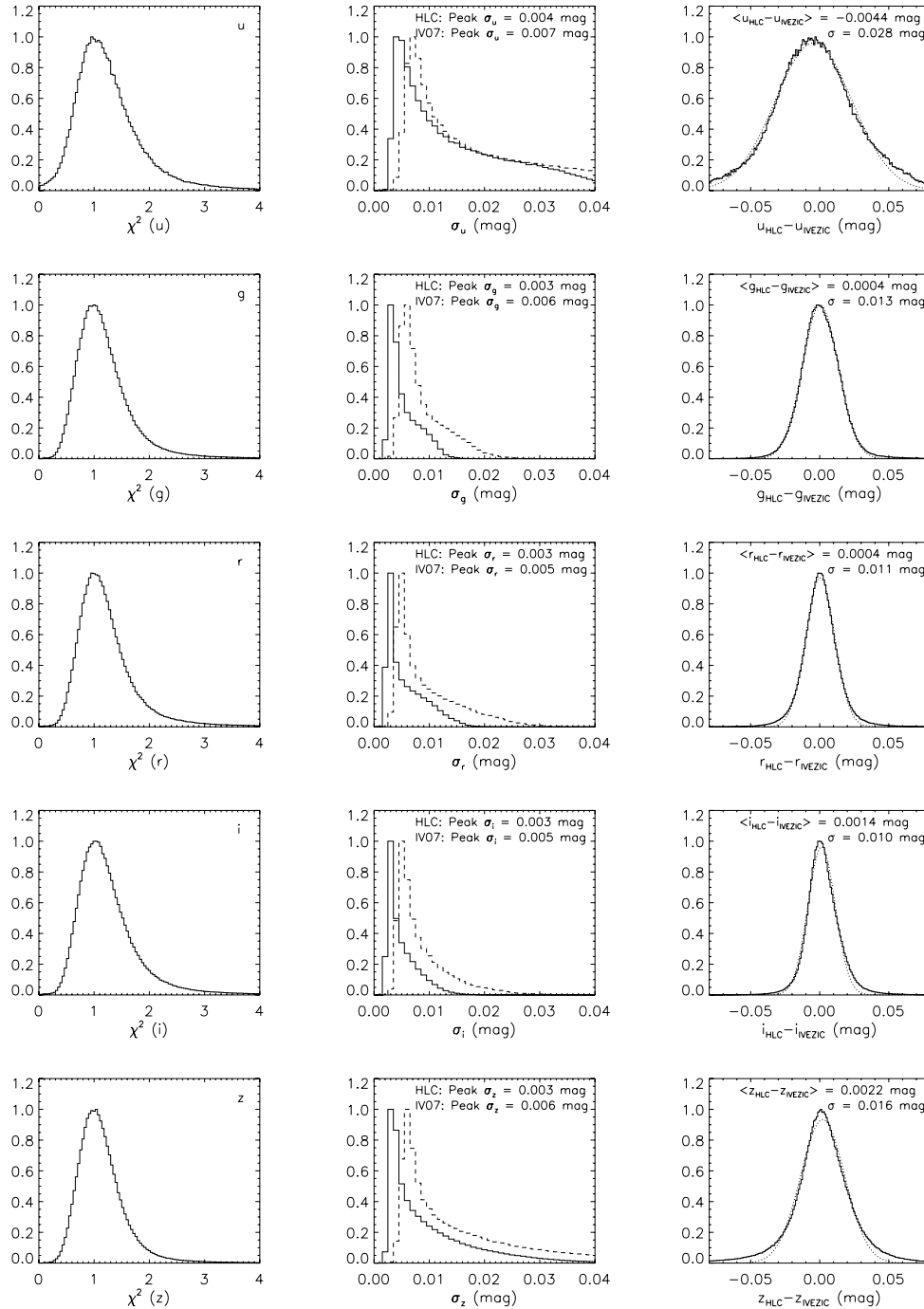
Figure 8. Each row of panels corresponds to a different waveband and the order employed is u, g, r, i and z from the top row to the bottom row. The LMCC objects used in the plots are matches with the IV07 standard star catalogue and have at least three good epochs with mean PSF magnitudes brighter than 21.5 mag in the u, g, r and i bands, and brighter than 20.5 mag in the z band. Left-hand column: Normalized histograms of χ^2 per degree of freedom for the mean PSF magnitudes in the HLC. Middle column: Normalized histograms of the uncertainties on the mean PSF magnitudes in the HLC (solid lines) and on the mean magnitudes from the IV07 catalogue (dashed lines). Right-hand column: Normalized histograms of the difference between the HLC mean PSF magnitudes and the IV07 catalogue mean magnitudes, along with a fitted Gaussian (dotted line).

using a very similar method to our recalibration of SDSS astrometry presented in Section 2.4.

We compare our proper motions in the HLC to those derived by GK04 for the 30 546 stars from their catalogue with an unambiguous positional match in the HLC using a match radius of 0.7 arcsec. In Fig. 9, we plot the running 3σ-clipped mean difference between our HLC proper motions and those of GK04 (middle points) as a

function of RA using a $1°$ window (upper panels), as a function of Dec. using a $0°.01$ window (middle panels), and as a function of mean r PSF magnitude using a 0.1-mag window (lower panels). The mean difference is only calculated if there are at least 100 stars in the sliding window. The left-hand panels correspond to proper motion in RA and the right-hand panels correspond to proper motion in Dec. We also plot the mean difference plus or minus the running
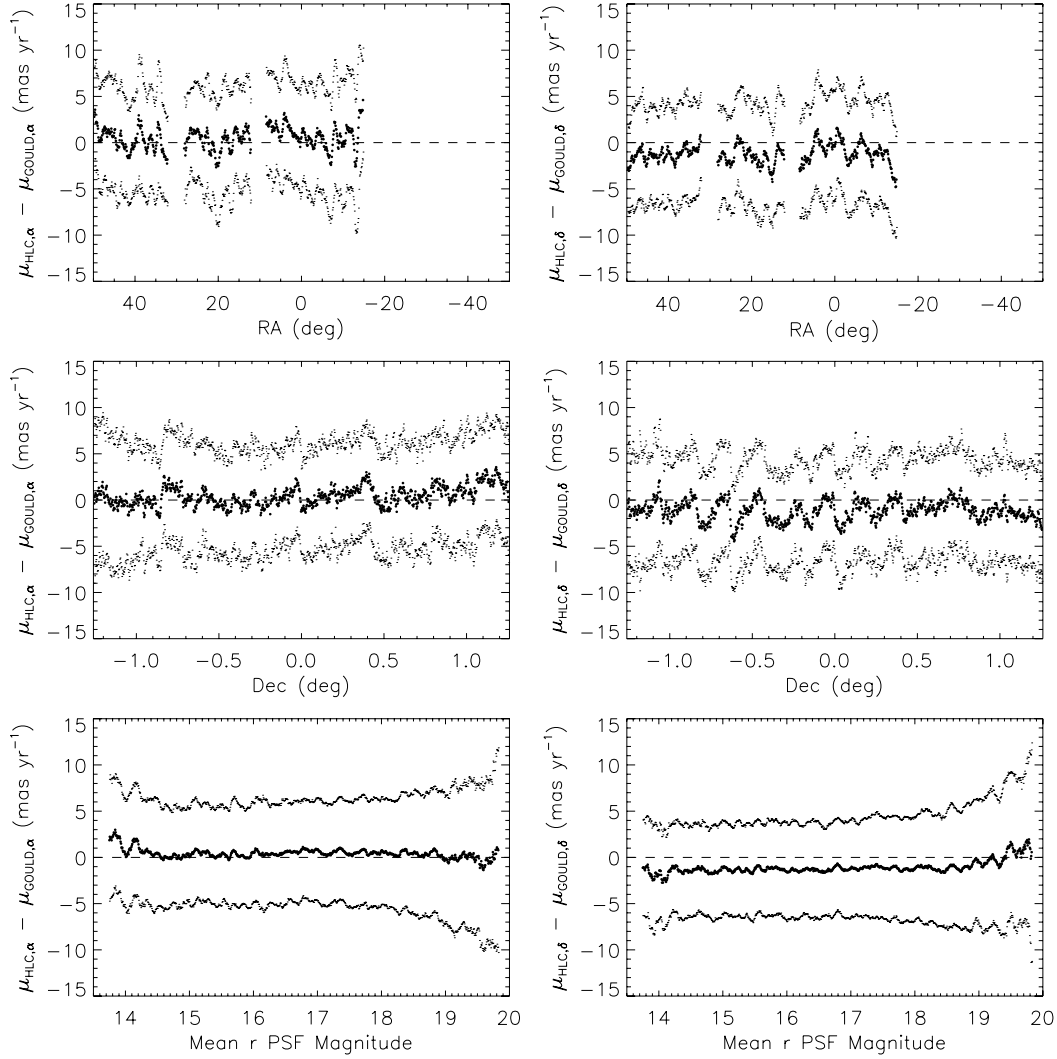
Figure 9. Plots of the running 3σ-clipped mean difference between the HLC proper motions and those of GK04 (middle points) as a function of RA using a $1°$ window (upper panels), as a function of Dec. using a $0°.01$ window (middle panels), and as a function of mean r PSF magnitude using a 0.1-mag window (lower panels). The left-hand panels correspond to proper motion in RA and the right-hand panels correspond to proper motion in Dec. The upper and lower sets of smaller points in each panel represent the mean difference plus or minus the running 3σ-clipped standard deviation, respectively.

3σ-clipped standard deviation as the upper and lower sets of smaller points, respectively, in each panel.

Fig. 9 illustrates that the systematic differences between the HLC proper motions and those of GK04 are at a very small level, generally $\lesssim 2$ mas yr^{-1}. We note one clear systematic trend that the GK04 Dec. proper motions are offset from the HLC Dec. proper motions by $\lesssim 2$ mas yr^{-1}, which is especially visible in the bottom right-hand panel of Fig. 9. We are currently unable to identify unambiguously the origin of the small systematic offset. The scatter in the proper motion differences (represented by the upper and lower sets of smaller points in each panel) is consistent with the stated proper motion uncertainties of $\sim$3.9 mas yr^{-1} in GK04, and $\lesssim 5$ mas yr^{-1} for these particular stars in the HLC.

Each light-motion curve in the LMCC has a different temporal coverage and number of epochs, a situation which is highlighted in Fig. 2. Consequently the uncertainties on the HLC proper motions exhibit a very inhomogeneous spatial distribution, and selecting proper motion objects using cuts on proper motion uncertainty results in a very inhomogeneous sample of objects. In Fig. 10, we present the mean proper motion uncertainty in the HLC as a func-

tion of mean r PSF magnitude, number of epochs and time-span of a light-motion curve for PSF-like objects (MEAN_OBJECT_TYPE = 6). The three panels from left- to right-hand side correspond to different light-motion curve time-spans of 3, 5 and 7 yr, respectively, while in each panel three curves are plotted, dotted dashed and continuous, corresponding to $\leqslant 10$, ≈ 20 and $\geqslant 30$ epochs, respectively. The curves in each panel show the mean proper motion uncertainty in the HLC as a function of mean r PSF magnitude. It is worth noting that $\sim$76 per cent of objects in the LMCC have at least 20 epochs, and that $\sim$37 per cent have at least 20 epochs with a time-span of greater than 4 yr. We find that 312 819 objects in the LMCC (or $\sim$8 per cent) have proper motions μ with $\mu/\sigma_\mu > 5$.

5 CONCLUSIONS

The LMCC contains almost 4 million light-motion curves for stars and galaxies covering $\sim$249 deg^2 in the SDSS Stripe 82. A light-motion curve provides waveband and time dependent photometric and astrometric quantities, where $\sim$76 per cent of light-motion curves in the LMCC have at least 20 epochs of measurements. The
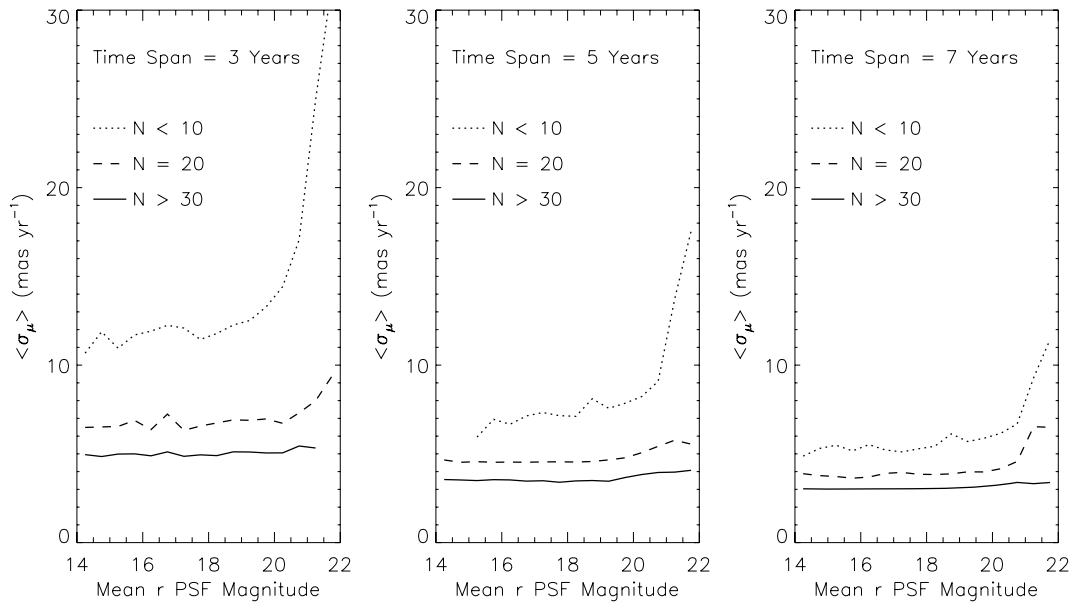
Figure 10. Plot of mean proper motion uncertainty in the HLC as a function of mean *r* PSF magnitude for PSF-like objects (stars). The left-hand, middle and right-hand panels correspond to light-motion curve time-spans of 3, 5 and 7 yr, respectively. In each panel, the dotted, dashed and continuous curves correspond to ⩽10, ≈20 and ⩾30 epochs, respectively.

LMCC is complete to magnitude 21.5 in *u, g, r* and *i*, and to magnitude 20.5 in *z*, making it the deepest large-area catalogue of its kind. The photometric rms accuracy for stars is ∼20 mmag at *r* ∼ 18 mag and for galaxies it is ∼30 mmag at *r* ∼ 18 mag. In both the RA and Dec. coordinates, an rms accuracy of ∼32 and 35 mas at *r* ∼ 18 mag is achieved for pre-2005 data for stars and galaxies, respectively, and an rms accuracy of ∼35 and 46 mas at *r* ∼ 18 mag is achieved for 2005 data for stars and galaxies, respectively.

The LMCC is thus an ideal tool for studying the variable sky, and in order to aid in its exploitation, we have created the HLC. The HLC consists of 229 derived photometric and astrometric quantities for each light-motion curve, and it is stored in a set of FITS binary tables, a format that is widely used by the astronomical community. The photometry presented in the HLC is fully consistent with the IV07 standard star catalogue and, since it is based on many more epochs, the random uncertainties in the mean magnitudes are smaller. Reassuringly, we show that only a very small percentage of standard stars (∼0.065 per cent or ∼650 objects) from IV07 are actually photometrically variable. The HLC proper motions of 30 546 stars are consistent to within uncertainties with those derived by GK04 by combining SDSS DR1 and USNO-B proper motions.

The power in using the HLC is well illustrated by the work of Vidrih et al. (2007) who construct a reduced proper motion diagram for Stripe 82 in order to find rare white dwarf populations, and consequently they identify eight new candidate ultracool white dwarfs and 10 new candidate halo white dwarfs. Also, Becker et al. (2008) report the discovery of an eclipsing M-dwarf binary system 2MASS J01542930+0053266, having employed the corresponding light-motion curve along with radial velocity measurements to determine the masses and radii of the stellar components. We therefore encourage the astronomical community to actively use and explore these catalogues that are so ample in their content.

ACKNOWLEDGMENTS

REFERENCES

Adelman-McCarthy J. K. et al., 2007, ApJS, 172, 634
Becker A. C. et al., 2004, ApJ, 611, 418
Becker A. C. et al., 2008, preprint (astro-ph/arXiv:0801.4474)

Bramich D. M. et al., 2005, MNRAS, 359, 1096
Cotton W. D., Tody D., Pence W. D., 1995, A&AS, 113, 159
Frieman J. et al., 2008, AJ, 135, 338
Fukugita M., Ichikawa T., Gunn J. E., Doi M., Shimasaku K., Schneider D. P., 1996, AJ, 111, 1748
Gould A., Kollmeier J. A., 2004, ApJS, 152, 103 (GK04)
Gunn J. E. et al., 1998, AJ, 116, 3040
Gunn J. E. et al., 2006, AJ, 131, 2332
Hogg D. W., Finkbeiner D. P., Schlegel D. J., Gunn J. E., 2001, AJ, 122, 2129
Hanisch R. J., Farris A., Greisen E. W., Pence W. D., Schlesinger B. M., Teuben P. J., Thompson R. W., Warnock A. III, 2001, A&A, 376, 359
Ivezić Ž et al., 2004, Astron. Nachr., 325, 583
Ivezić Ž et al., 2007, AJ, 134, 973 (IV07)
Kilić M. et al., 2006, AJ, 131, 582
Lupton R. H., Gunn J. E., Ivezić Ž., Knapp G. R., Kent S., 2001, in Harnden F. R. Jr, Primini F. A., Payne H. E., eds, ASP Conf. Ser., Vol. 238, Astronomical Data Analysis Software and Systems X. Astron. Soc. Pac., San Francisco, p. 269
Lupton R. H., Gunn J. E., Szalay A. S., 1999, AJ, 118, 1406
Monet D. G. et al., 1998, USNO-A2.0 Catalogue. US Naval Observatory, Flagstaff
Monet D. G. et al., 2003, AJ, 125, 984
Munn J. A. et al., 2004, AJ, 127, 3034
Paczyński B., 2000, PASP, 112, 1281
Pier J. R., Munn J. A., Hindsley R. B., Hennessy G. S., Kent S. M., Lupton R. H., Ivezić Ž., 2003, AJ, 125, 1559
Schlegel D. J., Finkbeiner D. P., Davis M., 1998, ApJ, 500, 525
Scranton R. et al., 2002, ApJ, 579, 48
Sesar B. et al., 2007, AJ, 134, 2236
Smith J. A. et al., 2002, ApJ, 123, 2121
Stetson P. B., 1996, PASP, 108, 851
Stoughton C. et al., 2002, AJ, 123, 485
Tucker D. et al., 2006, Astron. Nachr., 327, 821
Vidrih S. et al., 2007, MNRAS, 382, 515
Wells D. C., Greisen E. W., Harten R. H., 1981, A&AS, 44, 363
York D. G. et al., 2000, AJ, 120, 1579
Zacharias N. et al., 2000, AJ, 120, 2131

This paper has been typeset from a TeX/LaTeX file prepared by the author.